



Facile synthesis of Sn-doped MOF-5 catalysts for efficient photocatalytic nitrogen fixation

Lixia Li^{a,b}, Xiangyi Lv^a, Liujuan Jin^a, Kexin Du^a, Juhui Jiang^{a,*}, Xiaohua Zhao^a, Huijun Liang^{c,*}, Yuming Guo^a, Xiaobing Wang^{a,*}

^a Collaborative Innovation Center of Henan Province for Green Manufacturing of Fine Chemicals, Key Laboratory of Green Chemical Media and Reactions, Ministry of Education, School of Chemistry and Chemical Engineering, Henan Normal University, Xinxiang, Henan 453007, China

^b Interdisciplinary Nanoscience Center, Aarhus University, Aarhus C 8000, Denmark

^c School of Chemistry and Materials Engineering, Xinxiang University, Xinxiang, Henan 453003, China

ARTICLE INFO

Keywords:

Photocatalytic nitrogen fixation
Metal organic framework
MOF-5
Sn-doped
T-tube reactor

ABSTRACT

The utilization of $\text{Zn}_4\text{O}(\text{1,4-benzenedicarboxylate})_3$ metal-organic framework (MOF-5) as a photocatalyst remains a substantial challenge owing to the limited stability under humid conditions and the low photocatalysis efficiency. Herein, a series of Sn-doped MOF-5 (Sn-MOF-5) were designed and fabricated for the photocatalytic N_2 fixation using the specific T-tube photocatalysis reactor. Detailed characterization results illustrates that an appropriate amount of Sn^{4+} doping can not only enhance the specific surface area and reducing capacity of MOF-5, but also decrease the bandgap width and promote the separation of photogenerated carriers. Therefore, at a Zn:Sn ratio of 6, Sn-MOF-5 with the highest Sn^{4+} ratio shows superior catalytic performance with the ammonia (NH_3) yield achieved $3912.76 \mu\text{mol L}^{-1} \text{g}^{-1}$ after 5 h, and the chemical stability is almost no decay after 15 h of continuous photocatalysis. This may offer a new strategy for improving catalytic performance and stability of MOF through doping Sn^{4+} .

1. Introduction

Ammonia (NH_3) is the most common industrial chemical as a highly important fertilizer feedstock and hydrogen storage intermediate [1]. Currently, conventional Haber-Bosch process for hydrogenation of nitrogen (N_2) molecules still dominated the industrial production of NH_3 . Nevertheless, it requires elevated temperatures (300–500 °C) and high pressures (100–300 atm) due to the extraordinarily difficult dissociation of $\text{N}\equiv\text{N}$ triple bond (dissociation energy of 944 kJ mol^{-1}), resulting in the massive energy consumption and greenhouse gas emissions [2,3]. Therefore, exploring a green and cost-effective method for the production of NH_3 is highly desirable. Recently, opting efficient routes including electrocatalysis [4,5] and photocatalysis [6,7] have been developed to convert N_2 into NH_3 . Among the alternative methods, photocatalytic NH_3 production in the aqueous phase is more attractive due to the utilization of solar light under ambient conditions.

Numerous efforts are devoted in developing efficient photocatalysts for N_2 fixation, ranging from metal compounds to inorganic non-metallic compounds and organic semiconductor, such as metal oxides

and sulfides (e. g., TiO_2 , La/MoO_3 , Bi_2MoO_6 , Bi_2S_3 , CdS/Pt/RuO_2) [8–13], nonmetal compounds (e. g., C_3N_4 [14,15]), MOF and COFs [16], etc. Typically, photocatalysis occurs by absorbing light to generate electron-hole pairs, which then migrate to the photocatalyst surface and react with H^+ and N_2 dissolved in the aqueous solution. However, most photocatalytic systems display relatively poor efficiency, owing to the low light-absorption efficiency, fast charge-carrier recombination and weak chemisorption of N_2 in the photocatalysts [17,18]. Therefore, developing an innovative strategy is of tremendous interest for the effectively photocatalytic activation of N_2 molecules.

Metal-organic frameworks (MOFs), with large specific surface area and relatively low cost, have been widely explored as photocatalyst for the CO_2 reduction [19], hydrogen evolution [20,21], wastewater treatment [22], nitrogen fixation [23–26], and so on. Meanwhile, integrating the porous structure of MOF with different types of metal sites and organic ligand allows for the efficient adsorption and diffusion of guest molecules [27]. It means that the composition and structure of MOFs are very beneficial to be used as the photocatalysts. For instance, by concurrently constructing a spatial proximity to the photoactive

* Corresponding authors.

E-mail addresses: jiangjuhui@126.com (J. Jiang), 95lhj@163.com (H. Liang), wxb95@163.com (X. Wang).

<https://doi.org/10.1016/j.apcatb.2023.123586>

Received 2 October 2023; Received in revised form 23 November 2023; Accepted 2 December 2023

Available online 18 December 2023

0926-3373/© 2023 Elsevier B.V. All rights reserved.

linkers and achieving unique Ni(I) coordination environment in atomically dispersed Ni₁-S/MOF, the charge transfer was greatly accelerated and thereby photocatalytic H₂ production activity was promoted [28]. MOF-5 frameworks anchored with small-sized Ni particles (Ni@MOF-5) have been previously reported for exhibiting low over-potential and high efficiency in photocatalytic hydrogen evolution [29]. The 3D channel structure inherent in MOF-5 additionally provides effective pathways for charge collection and transport [30]. Whereas, most of the MOFs suffer from poor stability in water, even in the humid air [31,32]. For example, the reactivity and stability of metal-organic framework Zn₄O(1,4-benzenedicarboxylate)₃ (MOF-5) can only be maintained when exposed to < 4% water. More researches demonstrated that the issue of water stability is particularly relevant to the lattice energy [32]. When the lattice energy of MOF is low, as is the case with Zn²⁺, Cu²⁺, and Co²⁺, they tend to be generally unstable in aqueous solution. This limitation also restricts the wide applications of MOF in aqueous photocatalysis system.

MOF lattice is formed by metal-ligand coordination interaction and coulombic bonds, while the lattice energy of MOF arises from the interaction between metal centers and organic ligands. Accordingly, MOFs with high-valent metal ions such as the trivalent ions (Cr³⁺, Fe³⁺, Al³⁺, Ce³⁺ etc.), prototypical Zr-based (UiO-66) and Ti-based (NH₂-MIL-125) MOFs, usually exhibit higher stability [33,34]. By contrast, the doping of high-valent metal ions can provide high charge density, strengthen the metal-ligand bonds, and lead to a high coordination number of the metal center [34,35]. Therefore, much higher lattice energy and water stability are expected when the nodes have multiple positive charges. However, to date, only a few MOFs with tetravalent ions have been developed, while developing MOFs based on high-valent metal ions remains a big challenge [33].

Herein, Sn-doped MOF-5 with Sn⁴⁺ (Sn_{1/x}-MOF-5, x is the molar ratio of Zn/Sn) was rationally fabricated and applied for the photocatalytic N₂ reduction fixation into NH₃. Particularly, an appropriate amount of doped Sn can lead to decreased bandgap width and increased redox ability. Therefore, Sn_{1/6}-MOF-5 shows remarkably superior NH₃ yield rate of 782.6 μmol L⁻¹ g⁻¹ h⁻¹. Meanwhile, Sn_{1/6}-MOF-5 also shows relatively durable stability with negligible activity decay after 15 h of continuous photocatalysis.

2. Experimental section

2.1. Materials and chemical reagents

N-methyl pyrrolidone, salicylic acid, potassium sodium tartrate, sodium nitroprusside and terephthalic acid (H₂BDC, analytical grade, Macklin Co., Ltd.), Zn(NO₃)₂·6 H₂O (analytical grade, Kermel Co., Ltd.), SnCl₂·2 H₂O and dichloromethane (Sinopharm Chemical Reagent Co., Ltd.), and sodium hypochlorite and sodium hydroxide (Damao Chemical Reagent Co., Ltd.) were used without further purification.

2.2. Preparation of catalyst

2.2.1. Preparation of metal organic frameworks-5 (MOF-5)

MOF-5 was prepared following the previously reported procedures [36]. In detail, Zn(NO₃)₂·6 H₂O (5.40 mmol) was dissolved in N-methyl pyrrolidone (30 mL) by ultrasonic at room temperature for 15 min. Then terephthalic acid (2.00 mmol) was added to the solution under continuous ultrasonication for another 30 min. Subsequently, the resulting solution was transferred into a 100 mL Teflon-lined stainless-steel autoclave and heated at 110 °C for 12 h. After cooling to room temperature, the obtained suspension was separated by centrifugation and washed three times with N-methyl pyrrolidone and dichloromethane. The solid fraction was subsequently dried under vacuum at 60 °C for 5 h. The resulting sample was obtained and denoted as MOF-5.

2.2.2. Preparation of Sn_{1/x}-MOF-5 catalysts

For the synthesis of Sn_{1/x}-MOF-5 with the molar ratio of Zn/Sn of 6 (Sn_{1/6}-MOF-5), Zn(NO₃)₂·6 H₂O (5.40 mmol) was mixed with N-methyl pyrrolidone (30 mL) by ultrasonication at room temperature for 15 min, followed by adding 2.00 mmol terephthalic acid under continuous ultrasonication for another 30 min. After that, SnCl₂·2 H₂O (0.90 mmol) was added into the above solution and ultrasonic for 15 min. The resulting solution was transferred into a 100 mL autoclave, and then heated to 110 °C for 12 h. After that, the solid fraction was separated from the mixture by centrifugation, washed three times with N-methyl pyrrolidone and dichloromethane, and dried at 60 °C under vacuum for 5 h. The final catalyst of Sn_{1/6}-MOF-5 was obtained as a yellow powder. Sn_{1/7}-MOF-5 and Sn_{1/5}-MOF-5 were obtained by varying the amount of SnCl₂·2 H₂O of 0.78 and 1.08 mmol, respectively.

2.3. Characterization techniques

The crystalline phases of as-prepared samples were analyzed using powder X-ray diffraction (XRD) patterns. The XRD measurements were conducted on a Bruker Advance-D8 Multiflex diffractometer equipped with Cu Kα radiation at 45 kV and 40 mA in a scan range of 2θ = 5–80° with a step size of 0.02°. Field emission scanning electron microscope (FESEM) images were recorded using the FESEM SU8010 apparatus, operating at 5 kV. Inductively coupled plasma optical emission spectrometry (ICP-OES) measurements were performed on an Agilent 5110 spectrometer. Before measurement, 15 mg sample was digested in 5 mL of HNO₃/HCl (1/3) and diluted to 25 mL. N₂ adsorption and desorption isotherms were measured on a Micrometric ASAP 2020 system. Prior to the measurement, the sample was outgassed at 120 °C for 8 h. UV–vis diffuse reflectance spectroscopy (UV–vis DRS) was performed on a Lambda 950 spectrophotometer in the wavelength range of 200 to 800 nm using pure BaSO₄ as a reference material. X-ray photoelectron spectroscopy (XPS) measurements were carried out on an ESCA-LAB250Xi with Al-Kα and Mg-Kα anode as the excitation sources. Peak fitting was carried out with a Shirley background function. Photoluminescence (PL) and fluorescence lifetime measurements of catalysts were conducted on a Shimadzu FLS980 steady/transient fluorescence spectrophotometer. Electrochemical tests were performed using a CHI660E electrochemical working station from Shanghai CH Instruments Co., Ltd. Prior to the measurement, a mixture of catalyst (20 mg), ethanol (1 mL), Nafion (10 μL) and NMP (20 μL) was sonicated for 1 h. The mixture was then dropped onto the FTO photoelectrode and 0.5 M Na₂SO₄ was served as electrolyte, Pt foil as counter electrode and Ag/AgCl electrode as reference electrode. In situ diffuse reflectance infrared fourier-transform spectroscopy measurements (DRIFTS) were carried out using a PerkinElmer Spectrum 400 F Fourier-transform spectrometer. The electron paramagnetic resonance (EPR) spectra arising from solid Sn_{1/x}-MOF-5 samples were acquired using a Bruker Micro spectrometer at room temperature under visible-light irradiation.

2.4. Photocatalytic nitrogen fixation

Photocatalytic nitrogen fixation experiments were conducted using a homemade photochemical installation (Scheme S1) or an one-pot method in the quartz tube. The reactor was exposed to a 300 W Xe lamp (Beijing Perfectlight Co., Ltd., MICROSOLAR300) at room temperature. Prior to the photocatalysis experiments, fresh deionized water was purged with N₂ in the dark for 0.5 h to make the solution N₂-saturated. Typically, to achieve an efficient contact between reactant and catalyst, a N₂-saturated solution (50 mL) was continuously and steadily dropped onto the catalyst (20 mg) at a constant flow rate to contact with immobilized in a specifically designed lockable T-quartz tube, allowing for a top-down flow system. Simultaneously, N₂ was continuously bubbled onto the catalyst surface from the middle side of T-quartz tube. Subsequently, the mixture was exposed to visible light irradiation using the 300 W Xe lamp. To monitor the reaction progress, 1 mL of the

reaction solution was collected at regular intervals of 1 h.

The concentration of ammonium ion in the collected samples was quantified using the indophenol blue method. 1 mL of the obtained solution was sequentially mixed with three portions of aqueous solutions including: (1) 500 μ L of a salicylic acid-potassium sodium tartrate solution (5 wt% of salicylic acid, 5 wt% of potassium sodium tartrate, and 0.3 M NaOH solution), (2) 50 μ L of sodium nitroprusside (1 wt%) and (3) 50 μ L of sodium hypochlorite. After reaction for 1 h, the above solution was drawn out for UV-vis absorbance measurement at 697 nm to determine the concentration of generated ammonia by comparing the absorbance with a standard curve (refer to Fig. S2). After the photocatalytic reaction proceeded for 5 h, the catalyst was dried at 60 °C for 12 h, and then re-secured in the T-shaped quartz tube to be used for the next photocatalysis process, following the same method as described above.

Compared to the aforementioned photochemical installation,

photocatalytic nitrogen fixation was also carried out using the regular one-pot method. In this method, the catalyst (20 mg) was immersed in a N_2 -saturated solution (50 mL) with continuously bubbled N_2 in the quartz tube under stirring. The solution was irradiated with visible light using the 300 W Xe lamp. A 1 mL portion of the reaction solution was collected from the mixture and filtered through a 0.22 μ m filter membrane. The collected samples were then analyzed using the indophenol blue method to quantify the concentration of ammonia. After the photocatalytic reaction proceeded for 5 h, the catalyst was collected by filtration and dried at 60 °C for 12 h. Subsequently, the dried samples were immersed again in fresh N_2 -saturated solution (50 mL) under stirring, in preparation for the next photocatalytic cycle using the same method as described above.

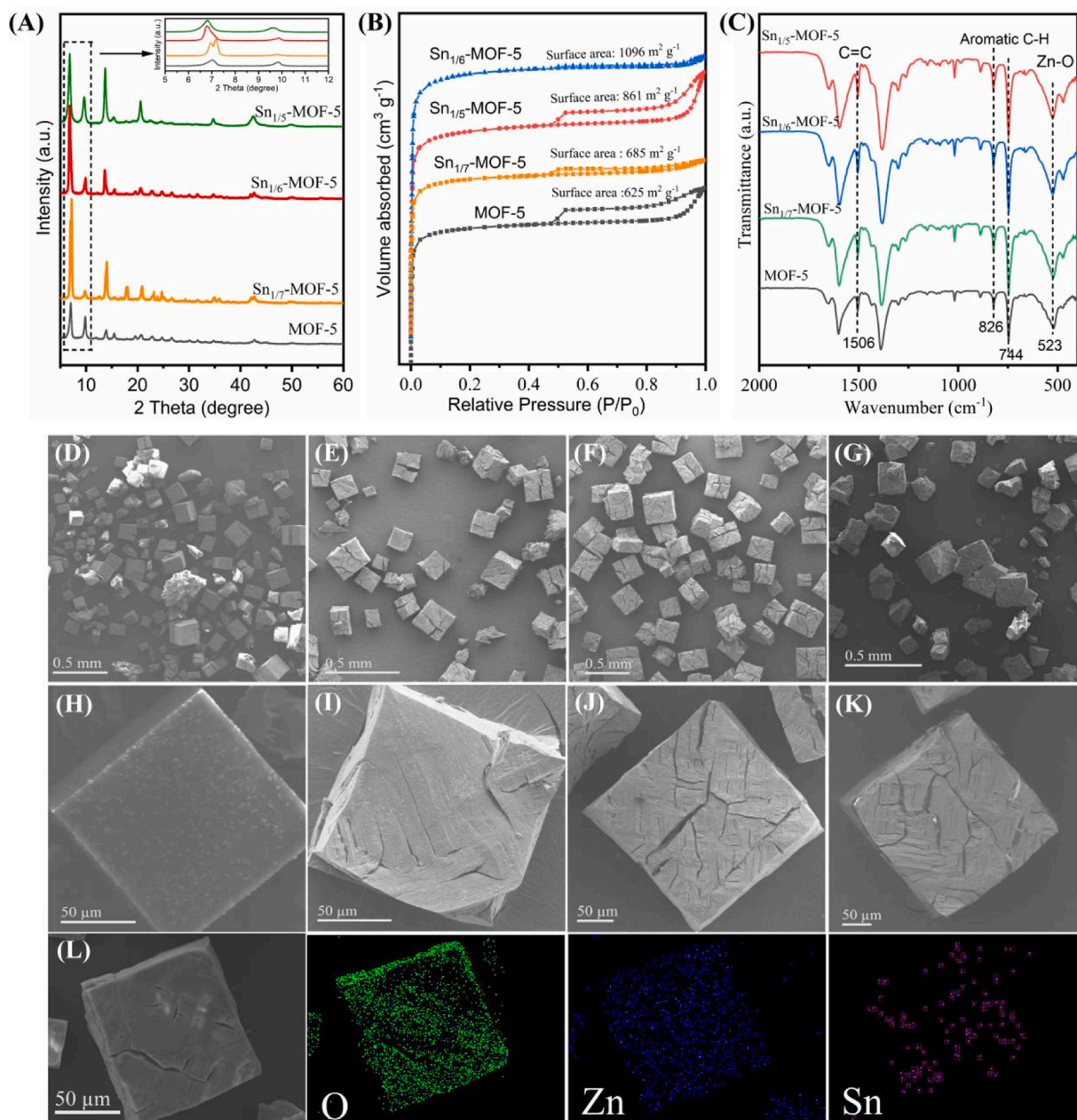


Fig. 1. (A) XRD patterns. (B) N_2 sorption isotherm. (C) FT-IR spectra. SEM images of (D, H) MOF-5, (E, I) $Sn_{1/7}$ -MOF-5, (F, J) $Sn_{1/6}$ -MOF-5, (G, K) $Sn_{1/5}$ -MOF-5 and (L) the corresponding EDS elemental mapping of $Sn_{1/6}$ -MOF-5.

3. Results and discussion

3.1. Morphological and structural characterizations

The crystal structures of the samples were initially characterized using XRD (Fig. 1 A). The distinct diffraction peaks of all samples observed at 6.9° , 9.6° , 13.7° and 15.3° match well with (200), (220), (400) and (420) crystal planes of MOF-5, respectively [37]. By contrast, the Sn-doped catalyst exhibits a higher diffraction peak on (200) and (400) planes compared to MOF-5, suggesting that the incorporation of minor quantity of Sn contributes to the enhancement of the (200) plane intensity. Nevertheless, as with an increase in the concentration of Sn, the intensity of 9.6° peak (corresponding to the (220) plane) gradually rises, while the intensity of the (200) plane experiences a decline from Sn_{1/7}-MOF-5 to Sn_{1/5}-MOF-5. Furthermore, as illustrated in the inset of Fig. 1a, the 6.9° peak position of Sn_{1/6}-MOF-5 shifts toward lower diffraction angles, indicating an expansion of lattice structure of MOF-5 due to Sn-doping [38]. In this regard, this phenomenon can be rationalized by the ionic radius and charge density of different oxidation states of Sn. In Sn-MOF-5, it is plausible that a portion of Sn²⁺ is oxidized to Sn⁴⁺ and Sn⁴⁺ possesses a higher charge density, consequently reinforcing the metal-ligand bonds. As a result, the intensity of (200) plane increases in comparison to that of MOF-5. However, it is essential to highlight that the ionic radius of Sn²⁺ (1.12 Å, while Sn⁴⁺ is 0.69 Å) considerably exceeds that of Zn²⁺ (0.74 Å) [39–41], so that the incorporation of Sn²⁺ into the MOF-5 lattice structure contributes to its expansion. Consequently, an increase in the Sn²⁺ concentration leads to a reduction in the intensity of the (200) plane, as observed.

ICP-OES confirmed that the Sn contents in the three Sn_{1/x}-MOF-5 samples were 1.10, 3.43 and 1.83 wt%, and the corresponding molar ratios of Zn to Sn are 26.21, 7.66 and 8.33 for Sn_{1/7}-MOF-5, Sn_{1/6}-MOF-5 and Sn_{1/5}-MOF-5, respectively (Table S1). Remarkably, the molar ratios of Zn to Sn in these samples are higher than the feeding ratios, particularly for Sn_{1/7}-MOF-5 sample. Interestingly, an increase in the Zn to Sn feeding ratios from 5 to 6 reveals an observation wherein the actual Zn/Sn ratios resist increase, concurrently accompanied by an increase in the Sn content. Correspondingly, Sn_{1/6}-MOF-5 with superior photocatalytic N₂ reduction shows the maximal Sn content and minimum actual Zn/Sn ratio. This is attributed to the change of crystal structure with an excessive theoretical doping of Sn, as obtained from the XRD results and decreased surface area (Figs. 1a and 1b). The N₂ sorption isotherms depicted in Fig. 1B for Sn_{1/x}-MOF-5 samples display a sharp increase at low relative pressures and characteristic type I isotherms, indicative of the micropore existence. Hysteresis between adsorption and desorption branches is evident at medium relative pressure for all the samples, signifying the presence of mesopores [42]. The nearly vertical tails of Sn_{1/6}-MOF-5 at the relative pressure near to 1.0 point to the existence of macroporosity. This observation markedly differs from the primarily microporous but negligibly meso-macroporous MOF-5 observed in prior studies [43,44], which is related to the hydrothermal treatment and heteroatom-doping are prone to causing the formation of meso-macroporosity. The corresponding pore size distribution curves of MOF-5 materials further affirm the prevalent presence of micro-mesopores (Fig. S2A–B). Notably, Sn_{1/7}-MOF-5 manifests two distinct sets of pore distributions, and the distribution centered at 0.7 nm is attributed to the intercalated structures [43]. With the exception of Sn_{1/7}-MOF-5, the other samples demonstrate a single pore size distribution centered at 1.2 nm (Fig. S2A). Particularly, Sn_{1/6}-MOF-5 boasts the largest pore volume recorded at $0.53 \text{ cm}^3 \text{ g}^{-1}$ (Table S1). Analysis of the N₂ sorption isotherms (Fig. S2A and Table S1) reveals that Sn_{1/x}-MOF-5 exhibits significantly augmented specific surface areas and pore volumes (Table S1) in comparison to MOF-5 ($625 \text{ m}^2 \text{ g}^{-1}$ and $0.35 \text{ cm}^3 \text{ g}^{-1}$, respectively). Remarkably, among the variants, Sn_{1/6}-MOF-5 showcases the most substantial specific surface area and pore volume of $1096 \text{ m}^2 \text{ g}^{-1}$ and $0.53 \text{ cm}^3 \text{ g}^{-1}$ respectively, along with the lowest average pore size of 1.95 nm. These findings indicate a higher

abundance of exposed adsorption and activation sites for N₂ upon Sn doping. Particularly noteworthy is the broader distribution observed in Sn_{1/6}-MOF-5, reveal a wider distribution, which serves to enhance the mass transfer pathway for N₂ and NH₃, consequently fostering improved photocatalytic performance.

The FT-IR spectra of Sn_{1/x}-MOF-5 in Fig. 1 C reveals the characteristic peaks at about 1577 and 1384 cm^{-1} corresponding to C–O stretching vibration of carboxylate in BDC²⁻, the peak at 1585 cm^{-1} assigned to asymmetric stretch vibration of carboxyl group, the peak at 1506 cm^{-1} representing C=C stretching vibration in aromatic of BDC²⁻, the peaks at 826 and 744 cm^{-1} ascribed to aromatic C–H out-of-plane deformation vibrations, the peaks at 648 , 808 and 1013 cm^{-1} attributed to bending vibration of C–H, the peak centered at 523 and 471 cm^{-1} ascribed to bending vibration of metal–O bond (Zn–O or Sn–O). The results of XRD and FT-IR illustrate that the introduction of Sn dopants did not lead to discernible alterations in the functional groups and composition of MOF-5 change with Sn dopants.

The distinct typical FESEM images, as depicted in Figs. 1D and 1H, distinctly illustrate the well-defined, regular cubic structure of MOF-5, characterized by its sleek surface. Upon Sn doping, the FESEM images reveal that Sn_{1/x}-MOF-5 samples still maintain a well-defined cubic morphology, and that discernible surface cracks become evident (Fig. 1E–I G). Remarkably, the extent of these surface cracks on the Sn_{1/x}-MOF-5 specimens progressively amplifies as the concentration of Sn increases, as showcased from Figs. 1I to 1 K, which can be attributed to the enlarged ionic radius and augmentation concentration of Sn²⁺. Additionally, the energy dispersive spectroscopy (EDS) elemental mapping images for Sn_{1/6}-MOF-5, depicted in Fig. 1 L, unequivocally manifest prominent signals corresponding to both Zn and Sn elements. This attests to the homogeneous dispersion of Sn dopants throughout the entirety of the sample. Consequently, it can be deduced that the partial substitution of Zn²⁺ ions within the framework by Sn²⁺ species, or the dissolution of Sn²⁺ into the MOF-5 lattice to form a Zn and Sn bimetal MOF-5 solid solution leads to the gradual escalation of surface cracks on the Sn_{1/x}-MOF-5 samples.

To reveal the local electronic structure, the XPS measurements are conducted (Fig. 2 and S2C). As shown in Fig. S2C, the characteristic Sn 3d_{3/2} peak partially overlaps with ZnO LMM Auger peak [45]. In Fig. 2A, the Sn 3d_{5/2} peak of Sn_{1/x}-MOF-5 can be fitted into Sn⁴⁺ (at $\sim 487.0 \text{ eV}$) and Sn²⁺ (at $\sim 486.5 \text{ eV}$) [46], and Sn_{1/6}-MOF-5 exhibited the maximum Sn⁴⁺/Sn²⁺ ratio (1.01) compared to Sn_{1/5}-MOF-5 (0.50) and Sn_{1/7}-MOF-5 (0.88). Additionally, Sn_{1/6}-MOF-5 showed the higher binding energy of Sn²⁺ (Fig. 2A), while Zn 2p peaks assigned to ZnO in Sn_{1/x}-MOF-5 shift to opposite direction (lower binding energy) upon the doping of Sn (Fig. 2B) compared to that in MOF-5, suggesting the decrease of local electron density of Sn due to the formation of Sn–O bond and the electronic transfer from Sn to Zn species. What's more, O 1s spectra of Sn_{1/x}-MOF-5 in Fig. 2C can be deconvoluted into three sub-peaks at about 531.2 (C–O), 532.2 (C=O) and 533.0 eV (oxygen atoms bonded to metals) [47]. Further investigation of the valence band (VB) from the XPS spectra in Fig. 2D reveals that the dope of Sn leads to a decreased localized charge accumulation and higher redox ability.

The assessment of photocatalytic nitrogen fixation performances of samples is conducted in a N₂-saturated aqueous environment, illuminated by a 300 W Xenon lamp. As depicted in Fig. 3 A, all examined samples manifest the generation of NH₄⁺. Specifically, the NH₄⁺ production for MOF-5, Sn_{1/7}-MOF-5, Sn_{1/6}-MOF-5 and Sn_{1/5}-MOF-5 are 240.5 , 1114.7 , 3912.8 and $1524.4 \mu\text{mol L}^{-1} \text{ g}^{-1}$, respectively. Particularly noteworthy is the exceptional photocatalytic activity exhibited by Sn_{1/6}-MOF-5, signifying approximately 16-fold increase in comparison to the MOF-5. It indicates a marked advancement in the photocatalytic nitrogen fixation performance of MOF-5 after Sn doping. Contrast experiments of Sn_{1/6}-MOF-5 performed under Ar atmosphere or in the dark, yielded negligible NH₄⁺, suggesting that NH₄⁺ originated exclusively from N₂ under light illumination rather than extraneous contaminants (Fig. 3 A). Therefore, the superior photocatalytic

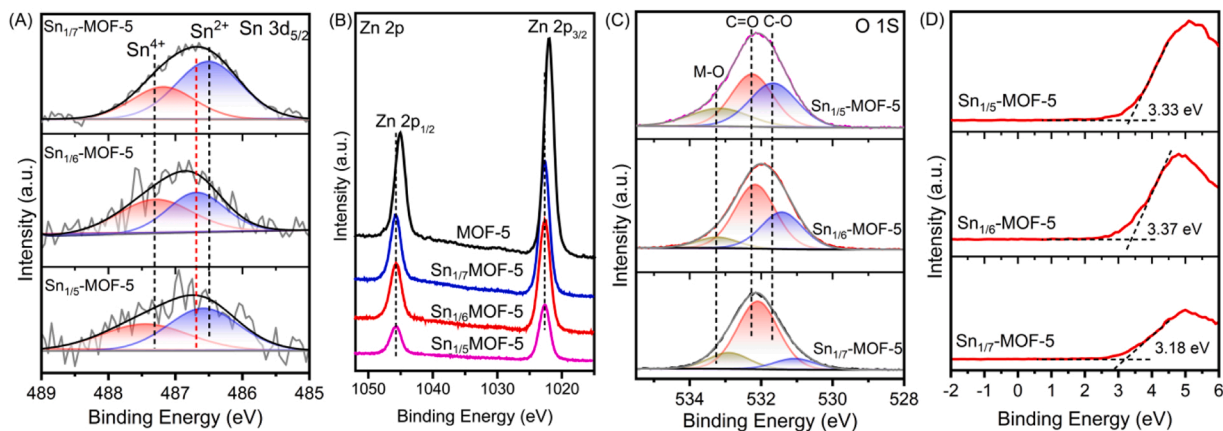


Fig. 2. XPS spectra of (A) Sn 3d, (B) Zn 2p, (C) O 1s, and (D) valence band spectra of $\text{Sn}_{1/x}\text{-MOF-5}$ catalysts.

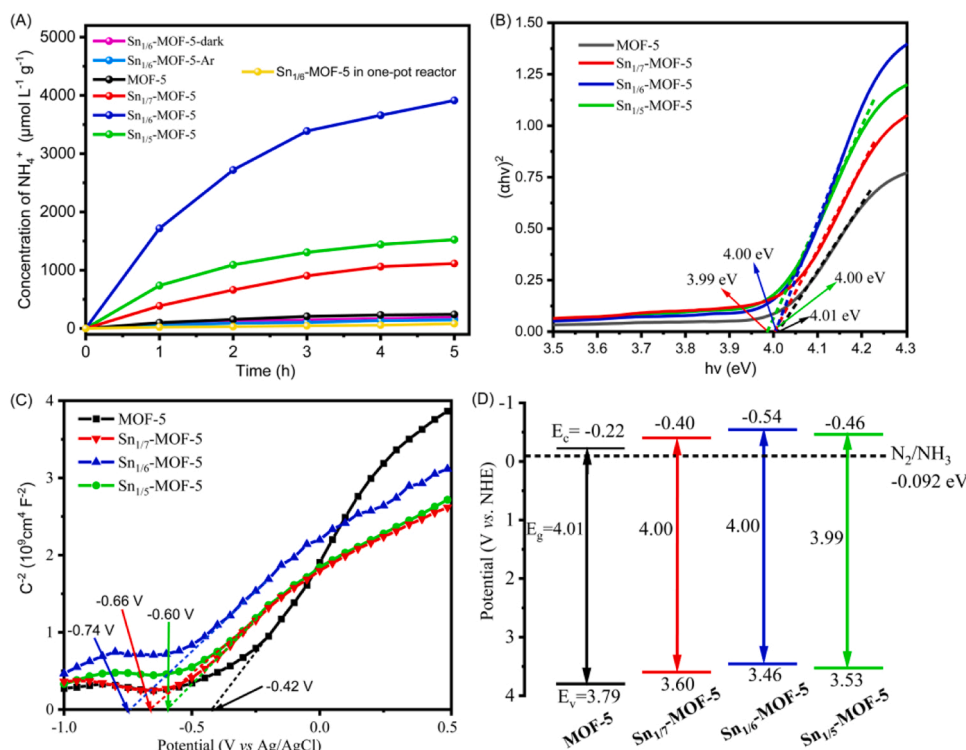


Fig. 3. (A) Photocatalytic activity of ammonia synthesis. (B) Corresponding spectra of $(\alpha h\nu)^2$ and $(h\nu)$. (C) Mott-Schottky plots. (D) Schematic diagram of the band gap of the materials.

performance demonstrated by $\text{Sn}_{1/6}\text{-MOF-5}$ is attributed to its heightened contact efficiency with N_2 and the enhanced mass transfer channel for N_2 and NH_3 according to the specific surface area and pore volume of samples (Fig. 1B and S2A-B).

3.2. The reaction mechanism of photocatalytic nitrogen fixation

To elucidate the mechanism of nitrogen fixation, a comprehensive experimental analysis was conducted focused on the optical absorption properties, the electronic band structures and the photogenerated charges dynamics. The UV-vis diffuse reflectance spectra of samples are determined and present in Fig. S3. All MOF-5-based samples exhibited prominent absorption intensity in the UV region while relatively weak absorption in the visible region. Remarkably, $\text{Sn}_{1/x}\text{-MOF-5}$ demonstrated heightened optical absorption intensity compared to MOF-5, while the range of optical adsorption remained largely unchanged.

Utilizing the Kubelka-Munk method, the band gaps of samples were calculated. Specifically, for MOF-5, $\text{Sn}_{1/7}\text{-MOF-5}$, $\text{Sn}_{1/6}\text{-MOF-5}$ and $\text{Sn}_{1/5}\text{-MOF-5}$, the calculated band gap values are 4.01, 4.00, 4.00 and 3.99 eV, respectively, suggesting that the dopant of Sn have only minimal impact on the band gaps of samples.

The electronic band structures, specifically the positions of the conduction band (CB) and valence band (VB), were determined experimentally using the Mott-Schottky plots (Fig. 3 C and 3D). The observed positive slopes in the Mott-Schottky plots for all samples are indicative of their n-type character. Notably, the introduction of dopant Sn leads to enhancements in both CB and VB positions, resulting in a more negative CB potential. This alteration facilitates the activation and reduction of nitrogen. Applying the Mott-Schottky equation at $1/C^2$ value of 0, a potential gap of 0.2 eV was selected. As a result, the conduction band minimum positions (ECBM) were calculated for MOF-5, $\text{Sn}_{1/7}\text{-MOF-5}$, $\text{Sn}_{1/6}\text{-MOF-5}$ and $\text{Sn}_{1/5}\text{-MOF-5}$ as -0.22 , -0.40 , -0.54 , and -0.46 eV

vs. the reversible hydrogen electrode potential (RHE), respectively. Particularly noteworthy is the substantial negativity of the CB potential exhibited by Sn_{1/6}-MOF-5, signifying its superior performance in N₂ fixation.

The dynamics of photoexcited electrons were meticulously evaluated through a combination of photocurrent measurements, electrochemical impedance, and fluorescence spectroscopy (Fig. 4). Fig. 4A illustrates the steady-state fluorescence spectra of samples, revealing that Sn_{1/6}-MOF-5 exhibits the minimum PL intensity at 518 nm owing to mitigation of photogenerated charge carrier recombination of Sn_{1/6}-MOF-5. Moreover, in Fig. 4B, compared to other samples, Sn_{1/6}-MOF-5 demonstrates the highest transient photocurrent value, underscoring its superior performance in photoexcited charge carrier generation. Complementing this, Fig. 4C displays a smaller arc radius for Sn_{1/6}-MOF-5, a clear indication of remarkably enhanced interfacial transfer efficiency of current carrier [48]. The time-resolved transient fluorescence spectra (Fig. 4D) provide further insights, revealing the longest fluorescence lifetime of 9.32 μ s for Sn_{1/6}-MOF-5, indicating that excited electrons are more likely to participate in N₂ fixation process before experiencing carrier recombination. Furthermore, the electron paramagnetic resonance (EPR) spectra of Sn_{1/x}-MOF-5 are shown in Fig. 4E and Fig. S5, both samples exhibited essentially identical paramagnetic absorption signals at $g = 2.005$ either in dark or under light, indicating the presence of the same type of unpaired electrons on π -conjugated aromatic heterocycles [49,50]. However, a significant decrease in the EPR signals was observed in Sn_{1/6}-MOF-5 compared to MOF-5. This observation suggests a lower density of structural defects and higher crystallinity upon the introduction of Sn, leading to a reduced density of unpaired electrons, which further illustrated an enhanced separation and transport of charge carriers at the contact interfaces [51,52]. These findings collectively emphasize that an optimal concentration of Sn dopant can markedly amplify the production of photoinduced electron, expedite interface charge transfer rate, and curtail the recombination of

photoinduced charge carrier, which are in strong agreement with the above-mentioned photocatalytic N₂ fixation results.

In the specific T-tube reactor, Sn_{1/6}-MOF-5 has exhibited noteworthy stability in ammonia production rate, sustaining a consistent NH₄⁺ concentration of 3521 μ mol g⁻¹ L⁻¹ after 5 cycles (Fig. 5A, red data point). In stark contrast, when subjected to photocatalysis within the quartz reactor under stirring conditions, Sn_{1/6}-MOF-5 displayed limited photocatalytic efficiency and stability during recycling experiments (Fig. 5A, black data point). This discrepancy is attributed to the deleterious effects of excess water molecules on the ZnO₄ tetrahedron, leading to the substitution of BDC O and inorganic O positions by water O atoms. This, in turn, diminishes the adsorption capacity of N₂. Observations from XRD spectra of Sn_{1/6}-MOF-5 during the photocatalysis process unveiled alterations in characteristic peaks, and the peak at 6.9° vanished and subsequently stabilized with prolonged illumination time (Fig. 5B). This phenomenon is likely attributable to a reduction in lattice parameter and partial phase transitions, resulting in a highly density state structure [53,54]. Furthermore, FT-IR spectra provide additional insights, illustrating the emergence characteristic peaks at 555 and 507 cm⁻¹ assigned to Zn-O or Sn-O bonds after 20 min of photocatalysis (Fig. 5C, panel d vs. panel b). This outcome confirms the formation of Zn-O or Sn-O bonds within the Sn_{1/6}-MOF-5 framework under the humid N₂ conditions, thereby corroborating the existence of ZnO and SnO₂ in a humid environment. The presence of a bond at 1405 cm⁻¹ can be attributed to the distinctive absorption of NH₄⁺ on Sn_{1/6}-MOF-5 in the presence of N₂ and water [55], compared to that with Ar and water, or solely with water (Fig. 5C, panel b vs. panel a and panel c). This direct confirmation establishes that NH₄⁺ indeed originates from N₂. Furthermore, the XPS spectra analysis of Sn 3d in Sn_{1/6}-MOF-5 reveals an increased Sn⁴⁺/Sn²⁺ peak area ratio, shifting from 1.01 to 1.83 (Fig. 5D). This change signifies an increase in SnO₂ species after reaction. Consequently, Sn_{1/x}-MOF-5 sample is capable of generating ZnO/SnO₂ or ZnO/SnO/SnO₂ heterojunction during the photocatalytic

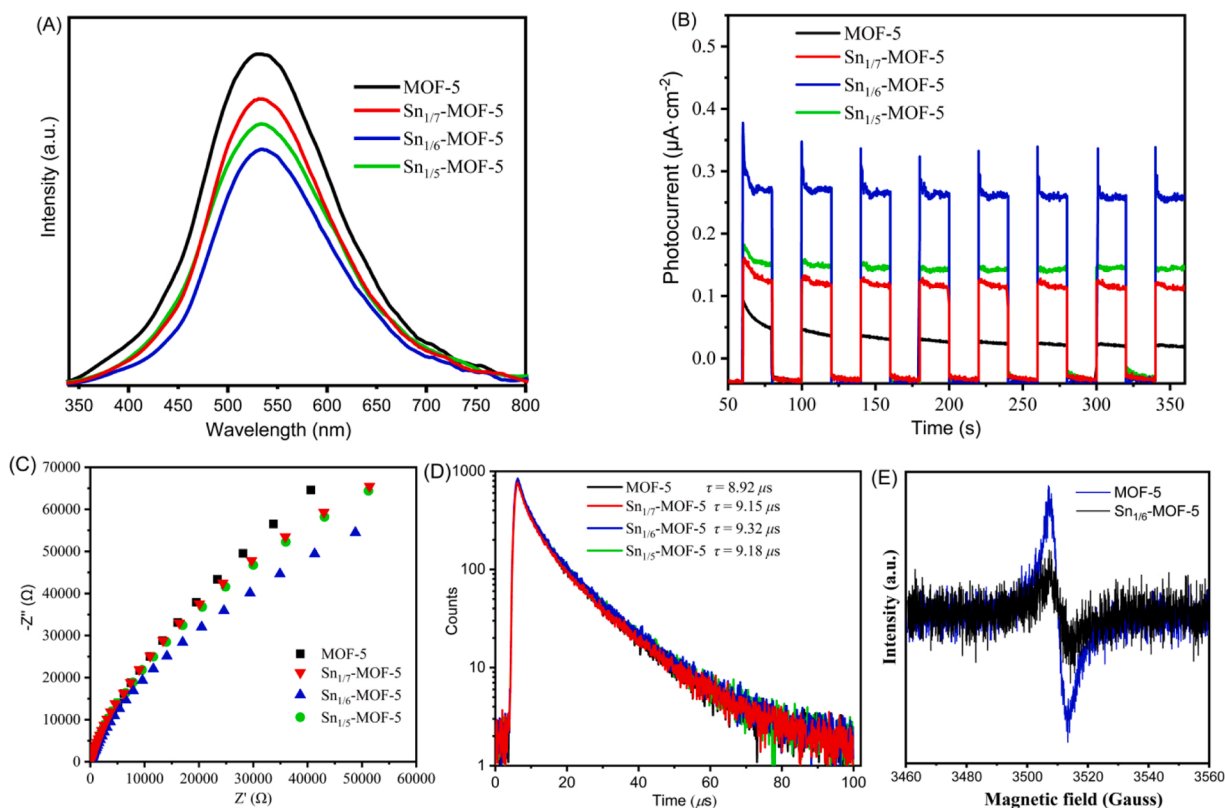


Fig. 4. (A) Steady-state fluorescence spectra. (B) The transient photocurrent. (C) The electrochemical impedance spectroscopy (EIS). (D) Time-resolved transient fluorescence spectra of samples. (E) EPR spectra of MOF-5 and Sn_{1/6}-MOF-5.

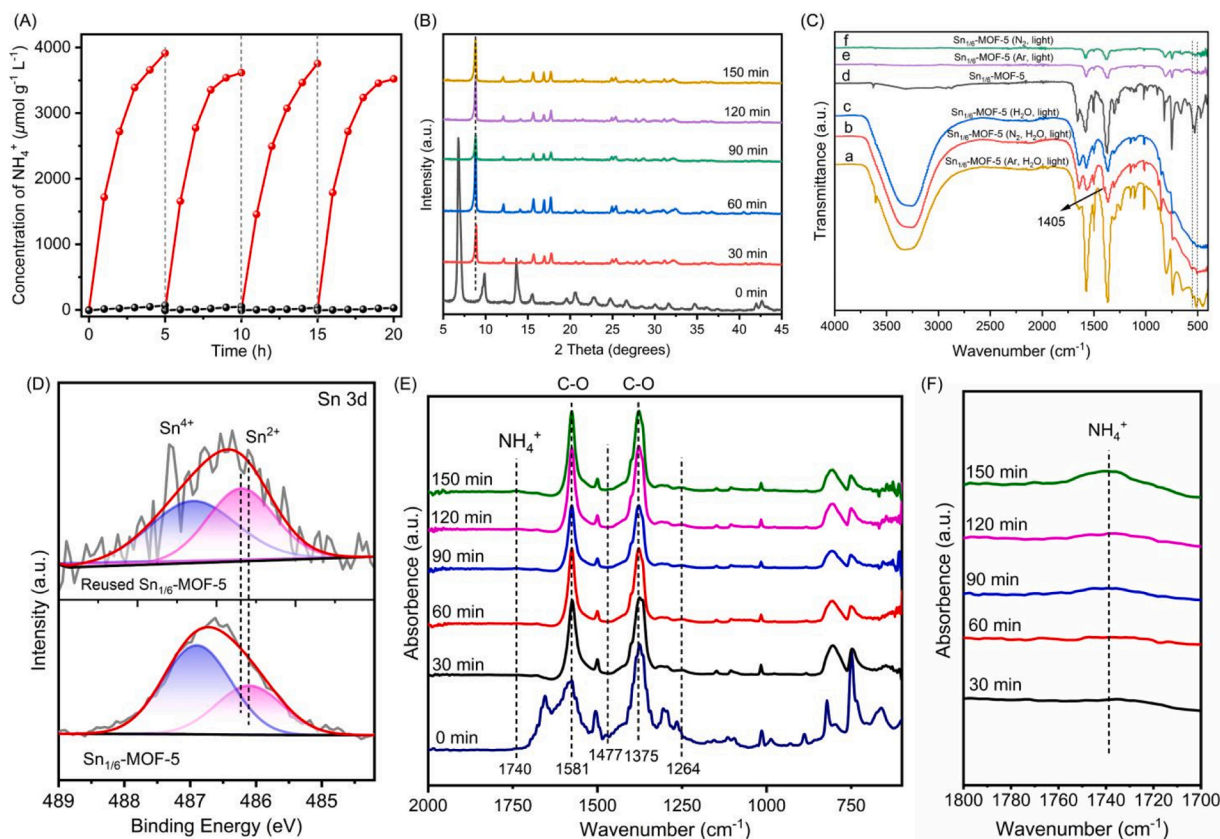


Fig. 5. Structural evolution of $\text{Sn}_{1/6}\text{-MOF-5}$ during the photocatalysis. (A) Cycling activity of $\text{Sn}_{1/6}\text{-MOF-5}$. (B–C) XRD and FT-IR spectra of $\text{Sn}_{1/6}\text{-MOF-5}$ at various reaction conditions. (D) XPS spectra of Sn 3d in $\text{Sn}_{1/6}\text{-MOF-5}$ before and after reaction. (E) In situ DRIFTS and (F) enlarged spectra recorded at different extended illumination time during N_2 photofixation over $\text{Sn}_{1/6}\text{-MOF-5}$.

process. This arrangement serves to enhance both photoinduced electron production and the interface charge transfer rate, thereby mitigating the recombination of photoinduced charge carrier.

To elucidate the mechanism of nitrogen fixation, in situ DRIFTS experiments were conducted (Fig. 5E–F). The infrared spectra of $\text{Sn}_{1/6}\text{-MOF-5}$ unveiled a series of discernible vibrational bands. These include peaks at 1375 and 1581 cm^{-1} , which correspond to the symmetric and asymmetric stretching vibrations of C–O bond within the $\text{C}_{10}\text{H}_{10}\text{O}_4$ group. Additionally, peaks at 826 and 744 cm^{-1} were attributed to out-of-plane bending vibration modes of the C–H bond, a characteristic feature of the benzene ring in the $\text{C}_{10}\text{H}_{10}\text{O}_4$ linker [56]. Upon exposure to visible light irradiation, a profound alteration in the IR signals was observed. Specifically, the characteristic peaks associated with -NH_2 (1624 cm^{-1}) exhibited a gradual decline, while the peak corresponding to the σ (N–H) bending mode within NH_4^+ (1740 and 1477 cm^{-1}) experienced a marked increase from enlarged spectra (Fig. 5F). This observation strongly implies the conversion of N–H to NH_4^+ [6,57]. Notably, the peak at 1129 cm^{-1} attributed to hydrazine, a pivotal intermediate product. This finding serves as compelling evidence that N_2 is adsorbed in a side-on bridging configuration, with subsequent nitrogen fixation occurring through the symmetric alternative pathway.

4. Conclusions

In summary, this study demonstrated that Sn-doped MOF-5 significantly enhances the adsorption ability of visible light and improves the separation and migration efficiency of photogenerated carriers, which helped to promote the adsorption of N_2 molecules. The obtained $\text{Sn}_{1/6}\text{-MOF-5}$ exhibited exceptional photocatalytic N_2 fixation performance, with an NH_4^+ yield of 3912.76 $\mu\text{mol L}^{-1} \text{g}^{-1}$ after 5 h in the specific T-tube reactor, which is nearly 50-fold higher than that achieved in one-

pot stirring reactor. This superior performance is ascribed to the appropriate Sn^{4+} dopant enhances the specific surface area and reducing capacity of MOF-5, and promotes the separation of photogenerated carriers, as well as facilitates the efficient contact between three-phase interfaces of water, catalyst and N_2 in the specific T-tube reactor. Additionally, the $\text{Sn}_{1/6}\text{-MOF-5}$ retains excellent chemical stability in 15 h of continuous photocatalysis. This study suggests new opportunities for the photochemical reduction of N_2 using MOF materials, providing promising prospects for future research in this field.

CRediT authorship contribution statement

Li Lixia: Conceptualization, Formal analysis, Funding acquisition, Investigation, Methodology, Writing – review & editing. **Wang Xiaobing:** Formal analysis, Validation, Writing – review & editing. **Guo Yuming:** Validation, Visualization. **Liang Huijun:** Investigation, Validation, Writing – review & editing. **Zhao Xiaohua:** Validation, Visualization. **Jiang Juhui:** Formal analysis, Methodology, Writing – review & editing. **Du Kexin:** Validation, Visualization. **Jin Liujuan:** Investigation, Validation, Visualization. **Lv Xiangyi:** Formal analysis, Methodology, Validation, Writing – review & editing.

Declaration of Competing Interest

The authors declare the following financial interests/personal relationships which may be considered as potential competing interests: Lixia Li reports financial support was provided by National Natural Science Foundation of China. Xiaobing Wang reports financial support was provided by Natural Science Foundation of Henan Province. Xiaobing Wang reports financial support was provided by Key Scientific Research Project of Colleges and Universities in Henan Province.

Data availability

Data will be made available on request.

Acknowledgements

The authors gratefully acknowledge the financial support of the National Natural Science Foundation of China (22308091), Natural Science Foundation of Henan Province (Grant No. 222300420511, 232102320202), Key Scientific Research Project of Colleges and Universities in Henan (No. 21A150027, 22A530002).

Appendix A. Supporting information

Supplementary data associated with this article can be found in the online version at doi:10.1016/j.apcatb.2023.123586.

References

- [1] B.H.R. Suryanto, K. Matuszek, J. Choi, R.Y. Hodgetts, H.-L. Du, J.M. Bakker, C.S. M. Kang, P.V. Cherepanov, A.N. Simonov, D.R. MacFarlane, Nitrogen reduction to ammonia at high efficiency and rates based on a phosphonium proton shuttle, *Science* 372 (2021) 1187–1191.
- [2] T. Liu, D. Zhai, B. Guan, Z. Shi, Nitrogen fixation and transformation with main group elements, *Chem. Soc. Rev.* 51 (2022) 3846–3861.
- [3] S.J.K. Forrest, B. Schluschaß, E.Y. Yuzik-Klimova, S. Schneider, Nitrogen fixation via splitting into nitrido complexes, *Chem. Rev.* 121 (2021) 6522–6587.
- [4] N. Zhang, L. Li, J. Wang, Z. Hu, Q. Shao, X. Xiao, X. Huang, Surface-regulated rhodium-antimony nanorods for nitrogen fixation, *Angew. Chem. Int. Ed.* 59 (2020) 8066–8071.
- [5] W. Guo, K. Zhang, Z. Liang, R. Zou, Q. Xu, Electrochemical nitrogen fixation and utilization: theories, advanced catalyst materials and system design, *Chem. Soc. Rev.* 48 (2019) 5658–5716.
- [6] G. Dong, X. Huang, Y. Bi, Anchoring black phosphorus quantum dots on Fe-doped $W_{18}O_{49}$ nanowires for efficient photocatalytic nitrogen fixation, *Angew. Chem. Int. Ed.* 61 (2022), e202204271.
- [7] Y.-H. Liu, C.A. Fernández, S.A. Varanasi, N.N. Bui, L. Song, M.C. Hatzell, Prospects for aerobic photocatalytic nitrogen fixation, *ACS Energy Lett.* 7 (2022) 24–29.
- [8] X. Liu, Y. Luo, C. Ling, Y. Shi, G. Zhan, H. Li, H. Gu, K. Wei, F. Guo, Z. Ai, L. Zhang, Rare earth La single atoms supported MoO_3-x for efficient photocatalytic nitrogen fixation, *Appl. Catal., B* 301 (2022), 120766.
- [9] H. Hirakawa, M. Hashimoto, Y. Shiraishi, T. Hirai, Photocatalytic conversion of nitrogen to ammonia with water on surface oxygen vacancies of titanium dioxide, *J. Am. Chem. Soc.* 139 (2017) 10929–10936.
- [10] X. Gao, L. An, D. Qu, W. Jiang, Y. Chai, S. Sun, X. Liu, Z. Sun, Enhanced photocatalytic N_2 fixation by promoting N_2 adsorption with a co-catalyst, *Sci. Bull.* 64 (2019) 918–925.
- [11] G. Wang, Q. Deng, H. Li, W. Hou, Mannitol and acidity co-tuned synthesis of oxygen-vacancy-modified bismuth molybdate nanorods for efficient photocatalytic nitrogen reduction to ammonia, *Sci. China Mater.* 66 (2023) 1435–1446.
- [12] G. Ren, M. Shi, Z. Li, Z. Zhang, X. Meng, Electronic metal-support interaction via defective-induced platinum modified BiOBr for photocatalytic N_2 fixation, *Appl. Catal., B* 327 (2023), 122462.
- [13] J. Yang, Progress of metal oxide (sulfide)-based photocatalytic materials for reducing nitrogen to ammonia, *J. Chem.* 2018 (2018) 3286782.
- [14] Z. Ding, S. Wang, S. Yan, Y. Zeng, D. Wang, Nano-SH-MOF@Self-assembling hollow spherical g-C₃N₄ heterojunction for visible-light photocatalytic nitrogen fixation, *ChemCatChem* (2023), e202201605.
- [15] R. Tong, Z. Sun, X. Zhong, X. Wang, J. Xu, Y. Yang, B. Xu, S. Wang, H. Pan, Enhancement of visible-light photocatalytic hydrogen production by $CeCO_3OH$ in g-C₃N₄/CeO₂ system, *ChemCatChem* 11 (2019) 1069–1075.
- [16] T. He, Z. Zhao, R. Liu, X. Liu, B. Ni, Y. Wei, Y. Wu, W. Yuan, H. Peng, Z. Jiang, Y. Zhao, Porphyrin-based covalent organic frameworks anchoring Au single atoms for photocatalytic nitrogen fixation, *J. Am. Chem. Soc.* 145 (2023) 6057–6066.
- [17] Y. Wei, W. Jiang, Y. Liu, X. Bai, D. Hao, B.-J. Ni, Recent advances in photocatalytic nitrogen fixation and beyond, *Nanoscale* 14 (2022) 2990–2997.
- [18] R. Shi, Y. Zhao, G.L.N. Waterhouse, S. Zhang, T. Zhang, Defect engineering in photocatalytic nitrogen fixation, *ACS Catal.* 9 (2019) 9739–9750.
- [19] J. Liang, H. Yu, J. Shi, B. Li, L. Wu, M. Wang, Dislocated bilayer MOF enables high-selectivity photocatalytic reduction of CO₂ to CO, *Adv. Mater.* 35 (2023) 2209814.
- [20] J. Yang, Y. Shen, Y. Sun, J. Xian, Y. Long, G. Li, Ir nanoparticles anchored on metal-organic frameworks for efficient overall water splitting under pH-universal conditions, *Angew. Chem. Int. Ed.* 62 (2023), e202302220.
- [21] Y.-N. Gong, T. Ouyang, C.-T. He, T.-B. Lu, Photoinduced water oxidation by an organic ligand incorporated into the framework of a stable metal-organic framework, *Chem. Sci.* 7 (2016) 1070–1075.
- [22] J. Tan, Z. Chen, C.H. Chen, M. Hsieh, A.Y. Lin, S.S. Chen, K.C.W. Wu, Efficient adsorption and photocatalytic degradation of water emerging contaminants through nanoarchitectonics of pore sizes and optical properties of zirconium-based MOFs, *J. Hazard. Mater.* 451 (2023), 131113.
- [23] L. Huang, X. Kong, K. Chang, Z. Yu, X. Tao, T. Tang, Y. Xu, DBD plasma assisted synthesis of MO@Fe/Ce-MOFs with rich oxygen defects as efficient photocatalysts for nitrogen fixation, *J. Environ. Chem. Eng.* 11 (2023), 109836.
- [24] W. Gao, X. Li, X. Zhang, S. Su, S. Luo, R. Huang, Y. Jing, M. Luo, Photocatalytic nitrogen fixation of metal-organic frameworks (MOFs) excited by ultraviolet light: insights into the nitrogen fixation mechanism of missing metal cluster or linker defects, *Nanoscale* 13 (2021) 7801–7809.
- [25] H. Huang, X. Wang, D. Philo, F. Ichihara, H. Song, Y. Li, D. Li, T. Qiu, S. Wang, J. Ye, Toward visible-light-assisted photocatalytic nitrogen fixation: A titanium metal organic framework with functionalized ligands, *Appl. Catal., B* 267 (2020), 118686.
- [26] L. Chen, Y. Hao, Y. Guo, Q. Zhang, J. Li, W. Gao, L. Ren, X. Su, L. Hu, N. Zhang, S. Li, X. Feng, L. Gu, Y. Zhang, A. Yin, B. Wang, Metal-organic framework membranes encapsulating gold nanoparticles for direct plasmonic photocatalytic nitrogen fixation, *J. Am. Chem. Soc.* 143 (2021) 5727–5736.
- [27] C. Wang, W. Lin, Diffusion-controlled luminescence quenching in metal-organic frameworks, *J. Am. Chem. Soc.* 133 (2011) 4232–4235.
- [28] X. Ma, H. Liu, W. Yang, G. Mao, L. Zheng, H.-L. Jiang, Modulating coordination environment of single-atom catalysts and their proximity to photosensitive units for boosting MOF photocatalysis, *J. Am. Chem. Soc.* 143 (2021) 12220–12229.
- [29] W. Zhen, J. Ma, G. Lu, Small-sized Ni(111) particles in metal-organic frameworks with low over-potential for visible photocatalytic hydrogen generation, *Appl. Catal., B* 190 (2016) 12–25.
- [30] P. Du, J. Schneider, P. Jarosz, R. Eisenberg, Photocatalytic generation of hydrogen from water using a platinum(II) terpyridyl acetylide chromophore, *J. Am. Chem. Soc.* 128 (2006) 7726–7727.
- [31] W. Zhang, Y. Hu, J. Ge, H.-L. Jiang, S.-H. Yu, A facile and general coating approach to moisture/water-resistant metal-organic frameworks with intact porosity, *J. Am. Chem. Soc.* 136 (2014) 16978–16981.
- [32] S. Navalón, A. Dhakshinamoorthy, M. Álvaro, B. Ferrer, H. García, Metal-organic frameworks as photocatalysts for solar-driven overall water splitting, *Chem. Rev.* 123 (2023) 445–490.
- [33] J. Zhu, P.-Z. Li, W. Guo, Y. Zhao, R. Zou, Titanium-based metal-organic frameworks for photocatalytic applications, *Coord. Chem. Rev.* 359 (2018) 80–101.
- [34] Y.-N. Gong, J.-H. Mei, J.-W. Liu, H.-H. Huang, J.-H. Zhang, X. Li, D.-C. Zhong, T.-B. Lu, Manipulating metal oxidation state over ultrastable metal-organic frameworks for boosting photocatalysis, *Appl. Catal., B* 292 (2021), 120156.
- [35] J.-X. Wang, J. Yin, O. Shekha, O.M. Bakr, M. Eddaoudi, O.F. Mohammed, Energy transfer in metal-organic frameworks for fluorescence sensing, *ACS Appl. Mater. Interfaces* 14 (2022) 9970–9986.
- [36] C. Dai, A. Zhang, M. Liu, Hollow alveolus-like nanovesicle assembly with metal-encapsulated hollow zeolite nanocrystals, *ACS Nano* 10 (2016) 7401–7408.
- [37] J. Hafizovic, M. Björger, U. Olsbye, P.D.C. Dietzel, S. Bordiga, C. Prestipino, C. Lamberti, K.P. Lillerud, The inconsistency in adsorption properties and powder XRD data of MOF-5 is rationalized by framework interpenetration and the presence of organic and inorganic species in the nanocavities, *J. Am. Chem. Soc.* 129 (2007) 3612–3620.
- [38] Y. Bo, H. Wang, Y. Lin, T. Yang, R. Ye, Y. Li, C. Hu, P. Du, Y. Hu, Z. Liu, R. Long, C. Gao, B. Ye, L. Song, X. Wu, Y. Xiong, Altering hydrogenation pathways in photocatalytic nitrogen fixation by tuning local electronic structure of oxygen vacancy with dopant, *Angew. Chem. Int. Ed.* 60 (2021) 16085–16092.
- [39] X. Zheng, L. Shen, F. Lin, Y. Xu, Q. Lin, L. Jiang, Bimetallic metal-organic frameworks MIL-53(xAl-yFe) as efficient catalysts for H₂S selective oxidation, *Inorg. Chem.* 61 (2022) 3774–3784.
- [40] J. Tu, W.-L. Song, H. Lei, Z. Yu, L.-L. Chen, M. Wang, S. Jiao, Nonaqueous rechargeable aluminum batteries: progresses, challenges, and perspectives, *Chem. Rev.* 121 (2021) 4903–4961.
- [41] D. Zeng, C. Yu, Q. Fan, J. Zeng, L. Wei, Z. Li, K. Yang, H. Ji, Theoretical and experimental research of novel fluorine doped hierarchical Sn₃O₄ microspheres with excellent photocatalytic performance for removal of Cr(VI) and organic pollutants, *Chem. Eng. J.* 391 (2020), 123607.
- [42] B. Liu, H. Shioyama, H. Jiang, X. Zhang, Q. Xu, Metal-organic framework (MOF) as a template for syntheses of nanoporous carbons as electrode materials for supercapacitor, *Carbon* 48 (2010) 456–463.
- [43] C. Chen, L. Meng, M.R. Alalouni, X. Dong, Z.-P. Wu, S. Zuo, H. Zhang, Ultra-highly active Ni-doped MOF-5 heterogeneous catalysts for ethylene dimerization, *Small* 19 (2023) 2301235.
- [44] X. Sun, T. Wu, Z. Yan, W.-J. Chen, X.-B. Lian, Q. Xia, S. Chen, Q.-H. Wu, Novel MOF-5 derived porous carbons as excellent adsorption materials for n-hexane, *J. Solid State Chem.* 271 (2019) 354–360.
- [45] J. Zuo, A. Erbe, Optical and electronic properties of native zinc oxide films on polycrystalline Zn, *Phys. Chem. Chem. Phys.* 12 (2010) 11467–11476.
- [46] J. Sun, Y. Hu, K. Liao, C. Tang, Y. Lang, J. Xu, L. Zhao, W. Zhou, Q. Wang, K. He, The effect of the Zn/Sn ratio on the formation of single phase kesterite Cu₂ZnSnS₄ solar cell material, *Ceram. Int.* 43 (2017) 8103–8108.
- [47] L. Wang, X. Li, Q. Li, X. Yu, Y. Zhao, J. Zhang, M. Wang, R. Che, Oriented polarization tuning broadband absorption from flexible hierarchical ZnO arrays vertically supported on carbon cloth, *Small* 15 (2019) 1900900.
- [48] J. Li, L. Cai, J. Shang, Y. Yu, L. Zhang, Giant enhancement of internal electric field boosting bulk charge separation for photocatalysis, *Adv. Mater.* 28 (2016) 4059–4064.
- [49] F. Guo, B. Hu, C. Yang, J. Zhang, Y. Hou, X. Wang, On-surface polymerization of in-plane highly ordered carbon nitride nanosheets toward photocatalytic mineralization of mercaptan gas, *Adv. Mater.* 33 (2021) 2101466.

- [50] G. Liu, G. Zhao, W. Zhou, Y. Liu, H. Pang, H. Zhang, D. Hao, X. Meng, P. Li, T. Kako, J. Ye, In situ bond modulation of graphitic carbon nitride to construct p-n homojunctions for enhanced photocatalytic hydrogen production, *Adv. Funct. Mater.* 26 (2016) 6822–6829.
- [51] J. Zhang, X. Liang, C. Zhang, L. Lin, W. Xing, Z. Yu, G. Zhang, X. Wang, Improved charge separation in poly(heptazine-triazine) imides with semi-coherent interfaces for photocatalytic hydrogen evolution, *Angew. Chem. Int. Ed.* 61 (2022), e202210849.
- [52] Q. Zhang, Y.-C. Chu, Z. Liu, M. Hong, W. Fang, X.-P. Wu, X.-Q. Gong, Z. Chen, Construction of triazine-heptazine-based carbon nitride heterojunctions boosts the selective photocatalytic C-C bond cleavage of lignin models, *Appl. Catal., B* 331 (2023), 122688.
- [53] J.A. Greathouse, M.D. Allendorf, The interaction of water with MOF-5 simulated by molecular dynamics, *J. Am. Chem. Soc.* 128 (2006) 10678–10679.
- [54] Y. Ming, N. Kumar, D.J. Siegel, Water adsorption and insertion in MOF-5, *ACS Omega* 2 (2017) 4921–4928.
- [55] J. Yang, Y. Guo, R. Jiang, F. Qin, H. Zhang, W. Lu, J. Wang, J. Yu, High-efficiency “working-in-tandem” nitrogen photofixation achieved by assembling plasmonic gold nanocrystals on ultrathin titania nanosheets, *J. Am. Chem. Soc.* 140 (2018) 8497–8508.
- [56] Y. Wu, H. Pang, W. Yao, X. Wang, S. Yu, Z. Yu, X. Wang, Synthesis of rod-like metal-organic framework (MOF-5) nanomaterial for efficient removal of U(VI): batch experiments and spectroscopy study, *Sci. Bull.* 63 (2018) 831–839.
- [57] S. Wang, X. Hai, X. Ding, K. Chang, Y. Xiang, X. Meng, Z. Yang, H. Chen, J. Ye, Light-switchable oxygen vacancies in ultrafine Bi₅O₇Br nanotubes for boosting solar-driven nitrogen fixation in pure water, *Adv. Mater.* 29 (2017) 1701774.